

# Heterogeneous Single-Atom Catalyst for Visible-Light-Driven High-Turnover CO<sub>2</sub> Reduction: The Role of Electron Transfer

Chao Gao, Shuangming Chen, Ying Wang, Jiawen Wang, Xusheng Zheng, Junfa Zhu, Li Song,\* Wenkai Zhang, and Yujie Xiong\*

Visible-light-driven conversion of CO<sub>2</sub> into chemical fuels is an intriguing approach to address the energy and environmental challenges. In principle, light harvesting and catalytic reactions can be both optimized by combining the merits of homogeneous and heterogeneous photocatalysts; however, the efficiency of charge transfer between light absorbers and catalytic sites is often too low to limit the overall photocatalytic performance. In this communication, it is reported that the single-atom Co sites coordinated on the partially oxidized graphene nanosheets can serve as a highly active and durable heterogeneous catalyst for CO<sub>2</sub> conversion, wherein the graphene bridges homogeneous light absorbers with single-atom catalytic sites for the efficient transfer of photoexcited electrons. As a result, the turnover number for CO production reaches a high value of 678 with an unprecedented turnover frequency of 3.77 min<sup>-1</sup>, superior to those obtained with the state-of-the-art heterogeneous photocatalysts. This work provides fresh insights into the design of catalytic sites toward photocatalytic CO<sub>2</sub> conversion from the angle of single-atom catalysis and highlights the role of charge kinetics in bridging the gap between heterogeneous and homogeneous photocatalysts.

Artificial photosynthesis is an intriguing approach to solar-to-chemical energy conversion, wherein solar energy is stored in chemical bonds as solar fuels.<sup>[1]</sup> In particular, the solar-driven conversion of CO<sub>2</sub> into energy-rich chemical fuels has attracted tremendous attention, considering its double benefits for enriching energy supply and mitigating CO<sub>2</sub> pollution.<sup>[2]</sup> As

traditionally classified into the two categories of catalysts that have been developed for photocatalytic CO<sub>2</sub> conversion, the homogeneous and heterogeneous photocatalysts distinctly exhibit their own strengths and weaknesses.<sup>[3]</sup> Homogeneous photocatalysts are known for their tunable light absorption with large coefficients as well as high activity and/or selectivity, benefiting from the atomically dispersed catalytic sites and versatile coordination forms.<sup>[4]</sup> However, homogeneous catalysts commonly suffer from the relatively costly and time-consuming synthesis as well as the difficult extraction and recycling for long-term use, which severely impedes their practical industrial applications.<sup>[5]</sup> In comparison, heterogeneous catalysts can largely overcome these limitations but their photocatalytic performance is yet to be improved. For this reason, it is an ideal solution toward the sustainable development of photocatalysis that the merits of both homogeneous and heterogeneous photocatalysts are combined together.<sup>[3c,d]</sup> As commonly recognized in previous attempts, this strategy has been proven as an extremely challenging task.

To combine the homogeneous and heterogeneous photocatalysis, we have to specifically address the three key steps in photocatalysis—light absorption, charge separation and transfer, and catalytic reactions. In terms of catalytic reactions, the heterogeneous single-atom catalysts that were first demonstrated in 2011<sup>[6]</sup> have recently sparked tremendous interest in various catalytic reactions<sup>[7]</sup> as they can bridge the gap between heterogeneous and homogeneous catalysis. In the single-atom catalysts, the individual and isolated metal atoms anchored on supports can be regarded as homogeneous catalyst analogs when the supports serve as rigid ligands from the viewpoint of coordination chemistry.<sup>[3b]</sup> This similarity offers the following advantages as compared with their nanocluster, nanoparticle, and bulk counterparts: (i) an unexpectedly high activity and selectivity by their unsaturated coordination sites and tunable electronic structures; (ii) a significant reduction in catalytic metal usage by maximizing the number of catalytic sites; and (iii) well-defined active sites for mechanistic studies. Previous studies on heterogeneous and homogeneous catalysts have suggested that earth-abundant Co is a promising catalytic

Dr. C. Gao, Dr. S. Chen, Y. Wang, J. Wang, Dr. X. Zheng, Prof. J. Zhu, Prof. L. Song, Prof. Y. Xiong

Hefei National Laboratory for Physical Sciences at the Microscale iChEM (Collaborative Innovation Center of Chemistry for Energy Materials)

School of Chemistry and Materials Science, National Synchrotron Radiation Laboratory, and CAS Center for Excellence in Nanoscience University of Science and Technology of China Hefei, Anhui 230026, P. R. China

E-mail: song2012@ustc.edu.cn; yxiong@ustc.edu.cn

Prof. W. Zhang  
Department of Physics  
Beijing Normal University  
Beijing 100875, P. R. China

The ORCID identification number(s) for the author(s) of this article can be found under <https://doi.org/10.1002/adma.201704624>.

DOI: 10.1002/adma.201704624

center for  $\text{CO}_2$  reduction;<sup>[4e,8]</sup> however, the reported turnover numbers (TONs) and turnover frequencies (TOFs) for heterogeneous Co photocatalysts (e.g., metal-organic frameworks<sup>[7h]</sup>) are still behind the records by homogeneous Co catalysts.

For this reason, we aim to tackle the limitations of traditionally catalysts for photocatalytic  $\text{CO}_2$  reduction based on single-atom Co catalysts. As a proof of concept, we employ a typical homogeneous photosensitizer  $[\text{Ru}(\text{bpy})_3]\text{Cl}_2$  as the light absorber, as it can offer a large absorption coefficient for visible light. To fully exploit the activity of single-atom Co sites for photocatalytic  $\text{CO}_2$  reduction, two key factors should be considered—the transfer of photoexcited electrons from light absorbers to catalytic Co sites that modulates the efficiency of entire photocatalytic system<sup>[3d]</sup> and the metal–support interactions that stabilize single metal atoms as well as alter their charge states.<sup>[9]</sup> Thus, the supports that bridge catalytic sites and light absorbers hold the key to achieving high photocatalytic performance. An ideal support should possess the following features: (i) specific anchoring sites to tightly “grasp” the single atoms; (ii) large surface area and flexible surface to allow the high loading of catalytic sites; and (iii) high carrier mobility to facilitate the photoexcited electron transfer.

In this communication, we demonstrate a simple thermal treatment approach to stably immobilize the isolated single Co atoms on the partially oxidized graphene nanosheets ( $\text{Co}_1\text{-G}$ ) for photocatalytic  $\text{CO}_2$  conversion. In our approach, the partially oxidized graphene plays dual roles in photocatalysis—offering C/O functional groups as a rigid ligand to anchor Co atoms and possessing relatively high conductivity to facilitate the transfer of photoexcited electrons from  $[\text{Ru}(\text{bpy})_3]\text{Cl}_2$  light absorber to catalytic Co sites, which well meets the criteria for supports above. With  $[\text{Ru}(\text{bpy})_3]\text{Cl}_2$  as a visible-light absorber, the efficient electron transfer enables the high-turnover photocatalytic  $\text{CO}_2$  reduction at the single-atom Co sites, which reaches an unprecedented TOF (up to  $3.77 \text{ min}^{-1}$ ) for heterogeneous catalyst. This work provides a promising approach to engineering the active sites for solar-driven  $\text{CO}_2$  conversion and highlights the key role of charge kinetics in photocatalysis at the intersection of homogeneous and heterogeneous systems.

Our model catalyst is formed by immobilizing the isolated single Co atoms on the partially oxidized graphene nanosheets (namely,  $\text{Co}_1\text{-G}$ ) through a simple thermal treatment process, as schematically illustrated in Figure 1a. In the process, graphene oxide (GO) and  $\text{Co}^{2+}$  cations are well mixed in water

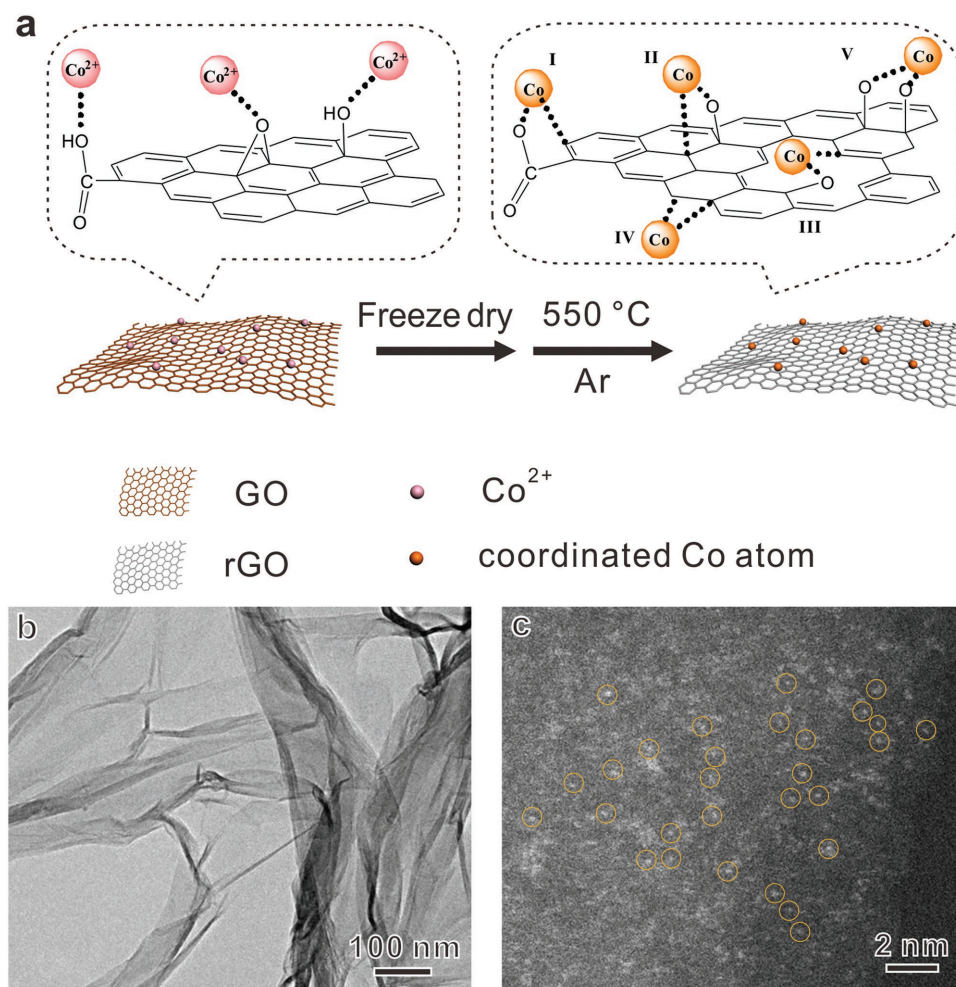


**Figure 1.** a) Schematic illustration for the synthetic procedure of the  $\text{Co}_1\text{-G}$  catalyst. b) TEM and c) HAADF-STEM images of the  $\text{Co}_1\text{-G}$  catalyst. The atomically dispersed Co atoms in (c) are highlighted by the yellow circles.

through sonication to prepare a precursor solution during which  $\text{Co}^{2+}$  cations adsorb onto the surface of GO due to the electrostatic force and complexation between the  $\text{Co}^{2+}$  cations and negatively charged oxygen-containing functional groups.<sup>[10]</sup> After freeze-drying to minimize the restacking of GO nanosheets, the  $\text{Co}_1\text{-G}$  catalyst can be obtained by heating the sample in Ar atmosphere.

During the process, GO is converted to reduced graphene oxide (rGO) via thermal deoxygenation as revealed by X-ray photoelectron spectroscopy (XPS; Figure S1, Supporting Information). Previous reports have demonstrated that annealing GO at 450 °C or above can provide an equivalent reducing ability to the chemical reduction with hydrazine monohydrate at 80 °C followed by heating at 200 °C.<sup>[11]</sup> It is worth noting that the reduction degree of rGO can influence its electric conductance.<sup>[12]</sup> To ensure an efficient electron transfer, the reduction degree of rGO should be kept high after the thermal deoxygenation. As illustrated in Figure S1b (Supporting Information), the peak intensities for oxygen-containing functional groups are dramatically reduced after the thermal deoxygenation for forming  $\text{Co}_1\text{-G}$ , indicating the high reduction degree of rGO. The removal of most oxygen-containing groups would enable higher electrical conductivity and thus allow the graphene nanosheets to serve as conductive channels, facilitating the transfer of photoexcited electrons. During the thermal deoxygenation, single Co atoms are tightly anchored to carbon and residual oxygen as evidenced by the following X-ray absorption fine structure (XAFS) characterization. Just like the

homogeneous catalysts, the isolated Co atoms coordinated on graphene surface are mostly present in +2 valence state. As determined by inductively coupled plasma mass spectrometry, the Co loading is 1.2 wt% on the graphene nanosheets.

The morphology of the  $\text{Co}_1\text{-G}$  catalyst is examined by transmission electron microscopy (TEM; Figure 1b) and scanning electron microscopy (SEM; Figure S2, Supporting Information). The TEM and SEM images show that the  $\text{Co}_1\text{-G}$  catalyst maintains the morphology of graphene nanosheets and possesses a sheet-like structure with corrugation and scrolling. In particular, we have not observed Co-derived clusters or particles on the nanosheets, suggesting that the Co species must be too tiny to be resolved by the ordinary mode of SEM and TEM techniques. To resolve information at an atomic scale, atomic-resolution aberration-corrected high-angle annular dark-field scanning TEM (HAADF-STEM; Figure 1c) is further used to characterize the  $\text{Co}_1\text{-G}$  nanosheets. As clearly revealed by Figure 1c, individual Co atoms are randomly dispersed on the graphene supports, which are highlighted by the yellow circles. As there are several possible anchoring modes for the isolated Co atoms to graphene (Figure 1a), it is imperative to precisely resolve the local structural information for Co atoms.

The samples are characterized by synchrotron radiation-based XAFS spectroscopy, a powerful technique for identifying the coordination structures of single Co atoms. Figure 2a show the Co K-edge X-ray absorption near-edge structure (XANES) spectra of the  $\text{Co}_1\text{-G}$  catalyst in reference to standard Co foil and CoO. The difference in intensity and position of the

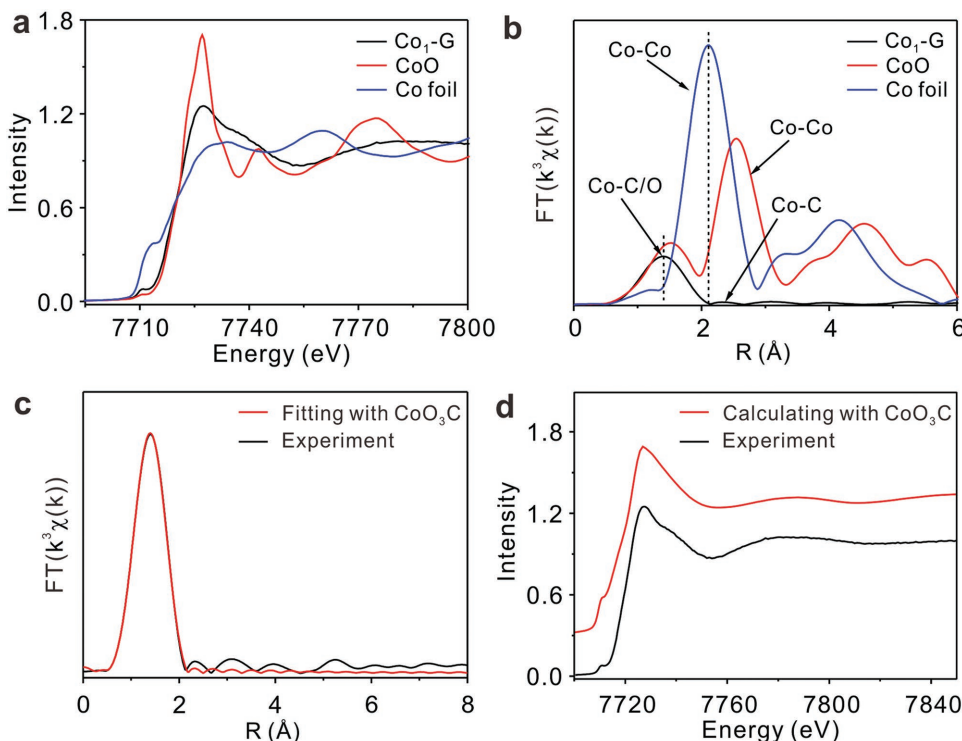


**Figure 2.** a) Normalized Co K-edge XANES spectra of the  $\text{Co}_1\text{-G}$  sample in reference to Co foil and CoO. b)  $k^3$ -weighted Fourier-transform Co K-edge EXAFS spectra. c) The comparison between the  $k^3$ -weighted Fourier-transform experimental EXAFS spectrum of the  $\text{Co}_1\text{-G}$  sample at Co K-edge (black line) and the fitting curves of  $\text{Co}_3\text{O}_4\text{C}$  coordination structure (red line). d) The comparison between the experimental XANES spectrum of the  $\text{Co}_1\text{-G}$  sample at Co K-edge (black line) and the theoretical spectra calculated for  $\text{Co}_3\text{O}_4\text{C}$  coordination structure (red line).

pre-edge peak at about 7711 eV implies that the Co atoms in the samples are of different environments. The white-line peak for  $\text{Co}_1\text{-G}$  at about 7727 eV is higher than that of Co foil but lower than that of  $\text{CoO}$ , indicating that the Co in  $\text{Co}_1\text{-G}$  possesses an electronic structure between those of  $\text{CoO}$  and Co foil. This observation suggests that Co atoms are positively charged through the charge transfer from Co to graphene, originating from the metal–support interactions. Processed through a Fourier transform (FT), the Co extended XAFS (EXAFS) spectra (Figure 2b) are obtained to determine the local structures of the single Co atoms. In reference to standard Co foil and  $\text{CoO}$ , the  $\text{Co}_1\text{-G}$  sample does not present the peak for Co–Co bond, suggesting the absence of Co-derived metallic Co or  $\text{CoO}$  clusters/particles. These results confirm that the Co species are isolated and dispersed single atoms. Meanwhile, the peak at about 1.4 Å for  $\text{Co}_1\text{-G}$  in EXAFS spectra indicates that the single Co atoms are coordinated with O or/and C atoms. To look into bonding information, we extract metal–metal bond lengths and metal coordination numbers from EXAFS curve fitting. As listed in **Table 1**, the coordination number (CN) of the isolated Co atoms in  $\text{Co}_1\text{-G}$  is 3.8, corroborating the coordinately unsaturated single Co atoms as compared with Co foil (CN = 12) and  $\text{CoO}$  (CN = 6).

The coordination structure of the  $\text{Co}_1\text{-G}$  is analyzed by fitting the  $k^3$ -weighted Fourier-transform EXAFS spectra (Figure 2c), which turns out to be more consistent with the four-coordinated  $\text{CoO}_3\text{C}$  configuration where the Co center atom is coordinated with three O atoms (Co–O, CN = 2.8) and one C atom (Co–C, CN = 1.0) at the graphene layer. As a matter of fact, we have ruled out the cases that the Co center atom is coordinated only with O atoms ( $\text{CoO}_4$ ) or with C atoms ( $\text{CoC}_4$ ) since the fitting results cannot reproduce the experimental spectrum well (Figure S3, Supporting Information). To further verify the four-coordinated  $\text{CoO}_3\text{C}$  configuration of  $\text{Co}_1\text{-G}$ , XANES calculations have been carried out for various four-coordinated structure models ( $\text{CoO}_4$ ,  $\text{CoO}_3\text{C}$ ,  $\text{CoO}_2\text{C}_2$ ,  $\text{CoOC}_3$ , and  $\text{CoC}_4$ ; Figure S4, Supporting Information). The calculation results for  $\text{CoO}_3\text{C}$  can reproduce the best main features of the experimental XANES spectrum (Figure 2d), which is consistent with the EXAFS fitting results. Overall, the Co is atomically dispersed at the graphene matrix, where both O and C atoms provide anchoring sites for the coordination with Co atoms. The obtained coordinately unsaturated single Co atoms may serve as excellent active sites toward excellent catalytic performance.

**Table 1.** Fitting results of Co K-edge EXAFS data. The lengths of Co–O, Co–C, and Co–Co bonds and coordination numbers of Co atoms are extracted from the curve fitting for Co K-edge EXAFS data (Figure 2). R, the lengths of Co–O, Co–C, and Co–Co bonds; CN, the coordination numbers of Co atoms;  $\sigma^2$ , the Debye–Waller factor. Error bounds (accuracies) are estimated as CN,  $\pm 5\%$ ; R,  $\pm 1\%$ ;  $\sigma^2$ ,  $\pm 1\%$ .

Sample	Bond	CN	R [Å]	$\sigma^2$ [ $10^{-3}$ Å $^2$ ]
$\text{Co}_1\text{-G}$	Co–C	1.0	1.68	1.5
	Co–O	2.8	1.96	8.9
$\text{CoO}$	Co–O	6.0	2.10	7.8
	Co–Co	12.0	3.01	8.9
Co foil	Co–Co	12.0	2.49	6.4

Upon acquiring the fine structures, we are now in a position to examine the performance of  $\text{Co}_1\text{-G}$  nanosheets as a catalyst for photocatalytic  $\text{CO}_2$  reduction. In order to evaluate the catalytic performance of single-atom Co sites at  $\text{Co}_1\text{-G}$  nanosheets, we choose a typical visible-light photosensitizer  $[\text{Ru}(\text{bpy})_3]\text{Cl}_2$  as the light absorber and triethanolamine (TEOA) as the sacrificial agent for photoexcited holes, which are commonly used in the homogeneous catalyst systems for photocatalytic  $\text{CO}_2$  reduction. **Figure 3a** summarizes the catalytic performance by our  $\text{Co}_1\text{-G}$  nanosheets in reference to control samples. Our  $\text{Co}_1\text{-G}$  catalyst (the last column in Figure 3a) achieves a TON of 374 and a TOF (turnover frequency) of  $2.08 \text{ min}^{-1}$  for CO production in the first 3 h, with a selectivity of 79.4% over competing  $\text{H}_2$  generation. Note that the synthesis gas products with a  $\text{CO}/\text{H}_2$  ratio between 0.5 and 1 are the desired gas sources for the thermochemical synthesis of methanol and Fischer–Tropsch reactions in the existing industrial processes,<sup>[13]</sup> suggesting the potential applications of our products. The CO product is continuously generated in the initial 3 h, but the yield rate gradually decreases as the reaction proceeds upon irradiation (Figure S5a, Supporting Information). This stagnation effect is attributed to the degradation of  $[\text{Ru}(\text{bpy})_3]\text{Cl}_2$  photosensitizer that has been reported in previous photocatalysis studies.<sup>[14]</sup> Encouragingly, the maximal TON of CO production can reach 678 (TOF,  $3.77 \text{ min}^{-1}$ ) through altering the ratio of  $[\text{Ru}(\text{bpy})_3]\text{Cl}_2$  to  $\text{Co}_1\text{-G}$  nanosheets (Figure S5b, Supporting Information), which is obviously higher than those of the state-of-the-art heterogeneous photocatalysts for  $\text{CO}_2$  reduction in literature (Table S1, Supporting Information). This indicates that the number of photoexcited electrons supplied to catalytic Co sites holds the key to the overall photocatalytic performance. Meanwhile, no liquid hydrocarbon products derived from  $\text{CO}_2$  such as  $\text{CH}_3\text{OH}$ ,  $\text{HCHO}$ , and  $\text{HCOOH}$  can be detected through analyzing the solvent after photocatalytic reactions by gas chromatograph and  $^1\text{H-NMR}$  spectroscopy (Figure S6, Supporting Information).

To further identify the key factors for high performance, we conduct a series of control experiments for performance comparison with  $\text{Co}_1\text{-G}$  nanosheets. As illustrated Figure 3a, the graphene without Co atoms anchored (G, the first column) exhibits a negligible TON of 0.2 for CO production and a low selectivity of 1.1% over competing  $\text{H}_2$  generation. Apparently, the isolated Co atoms in the  $\text{Co}_1\text{-G}$  catalyst are the catalytic sites for  $\text{CO}_2$  reduction. Although graphene does not provide active sites for  $\text{CO}_2$  reduction, it plays a key role in promoting the transfer of photoexcited electrons. When free  $\text{Co}^{2+}$  cations ( $\text{CoCl}_2$ , the second column) and  $\text{Co}^{2+}$  cations physically adsorbed at GO surface ( $\text{CoCl}_2 + \text{GO}$ , the fourth column) are adopted as catalysts under the same conditions, low TONs of 32 and 41 for CO production are obtained, respectively. In comparison, when  $\text{Co}^{2+}$  cations physically adsorbed at graphene surface ( $\text{CoCl}_2 + \text{G}$ , the third column) is used as a catalyst, the TON for CO production is obviously enhanced. These results demonstrate that the graphene, whose relatively high conductivity may facilitate the transfer of photoexcited electrons from  $[\text{Ru}(\text{bpy})_3]\text{Cl}_2$  to catalytic Co sites, enhances the overall photocatalytic performance. A previous work has employed MOF-253 as a support for the construction of catalytic active Ru complex for  $\text{CO}_2$  reduction, in which the MOF-253 plays a similar role in

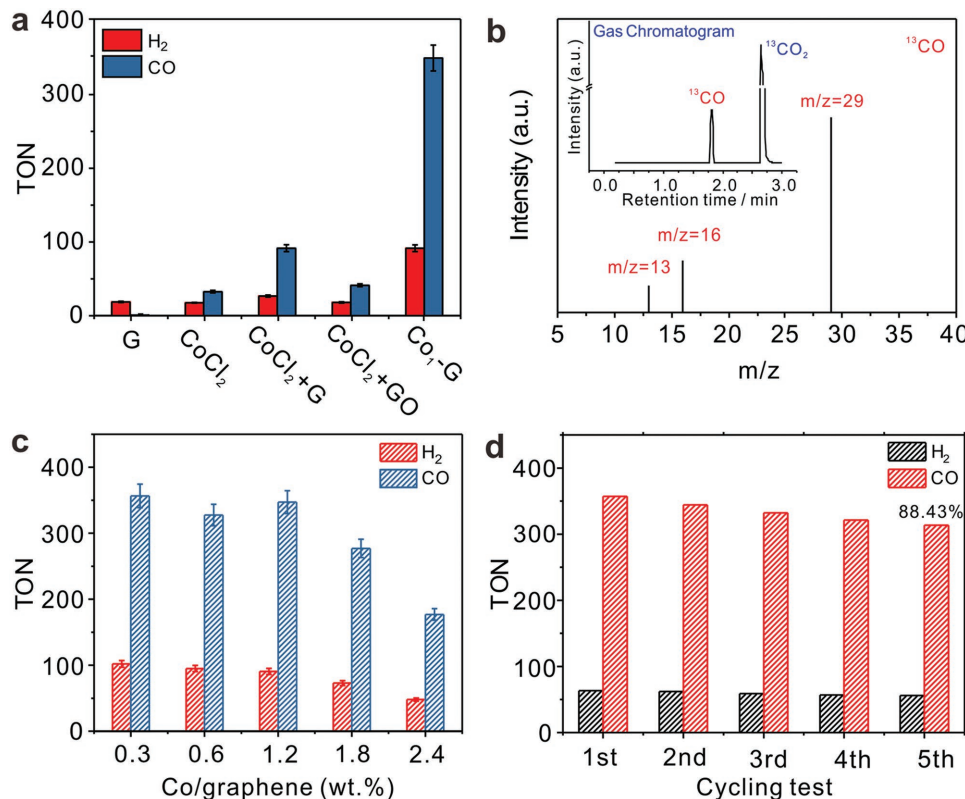


**Figure 3.** a) TONs of CO and  $\text{H}_2$  production by  $\text{Co}_1\text{-G}$  nanosheets in the first 3 h under visible-light ( $\lambda > 420$  nm) irradiation, in comparison with those by graphene (G),  $\text{CoCl}_2$ , graphene with  $\text{CoCl}_2$  ( $\text{CoCl}_2 + \text{G}$ ), and graphene oxide with  $\text{CoCl}_2$  ( $\text{CoCl}_2 + \text{GO}$ ) under the same condition.  $[\text{Ru}(\text{bpy})_3]\text{Cl}_2$  is used as a light absorber in all the measurements. b) GC-MS analysis of the carbon products using  $\text{Co}_1\text{-G}$  nanosheets as a catalyst in the photocatalytic reduction of  $^{13}\text{CO}_2$ . c) TONs of CO and  $\text{H}_2$  production in the first 3 h by altering the loading amounts of Co in  $\text{Co}_1\text{-G}$  nanosheets. d) TONs of CO and  $\text{H}_2$  production in the first 3 h using  $\text{Co}_1\text{-G}$  nanosheets as a catalyst in cycling tests. Each cycle takes 3 h.

facilitating the electron transfer from photosensitizers to catalytic active Ru centers.<sup>[15]</sup>

Indeed, the charge transfer is one important rate-limiting process in the overall photocatalytic reaction. Previous works have proven that ultrafast charge transfer can occur through  $\pi-\pi$  interfacial interactions.<sup>[16]</sup> In our system, the graphene nanosheets may provide the conductive channels for facilitating the photoexcited electron transfer toward the supported single Co sites through  $\pi-\pi$  interfacial interactions between the light absorber  $[\text{Ru}(\text{bpy})_3]\text{Cl}_2$  and graphene. This electron transfer process is more efficient than the case of free  $\text{Co}^{2+}$  cations without graphene whose electron transfer requires the collision between light absorbers and free  $\text{Co}^{2+}$  cations. As compared with graphene, the oxygen-containing functional groups in GO greatly break the conductive channels for electron transfer so that the  $\text{Co}^{2+}$  cations adsorbed at GO (i.e.,  $\text{CoCl}_2 + \text{GO}$ ) show a lower TON.

Here, we should point out that the physical adsorption of  $\text{Co}^{2+}$  cations to graphene largely limits the efficiency of electron transfer from graphene to  $\text{Co}^{2+}$  cations. The physically adsorbed sample ( $\text{CoCl}_2 + \text{G}$ , the third column in Figure 3a) exhibits a TON of 91 for CO production, only about 26% of the value with respect to  $\text{Co}_1\text{-G}$  nanosheets. In our  $\text{Co}_1\text{-G}$  catalyst, the isolated Co atoms are coordinated with carbon and residue oxygen at the surface of graphene, which are accomplished by annealing the system of  $\text{Co}^{2+}$  cations and GO. Such

a significant difference in catalytic performance emphasizes the importance of strong metal–support interactions to the electron transfer and thus the  $\text{CO}_2$  activation. Overall, the highly efficient  $\text{CO}_2$  conversion using a visible-light absorber is achieved by coupling single Co catalytic sites with partially oxidized graphene—a support enabling high electron mobility and strong metal–support interactions.

To verify the origin of produced CO, the isotopic  $^{13}\text{CO}_2$  is used as the reactant to trace the carbon sources in the photocatalytic reaction, and the obtained products are identified by gas chromatography-mass spectrometry (GC-MS; Figure 3b). The GC peak appearing at 1.8 min, corresponding to the  $m/z = 29$  in MS, is assigned to the generated  $^{13}\text{CO}$ , while the peak at 2.6 min is ascribed to the original  $^{13}\text{CO}_2$ . This result confirms that the produced CO indeed originates from  $\text{CO}_2$ . To investigate the effect of Co loading contents on the catalytic activity, the  $\text{Co}_1\text{-G}$  catalysts with the Co contents ranging from 0.3 to 2.4 wt% are prepared as reference samples. As evidenced in Figure 3c, the TONs are maintained nearly consistent when the Co loading contents are varied from 0.3 to 1.2 wt%, suggesting that every single Co atoms have been fully exploited as catalytic sites for  $\text{CO}_2$  reduction. However, when the Co loading contents exceed 1.2 wt%, the TONs are gradually reduced. A distinct decrease in TON is observed when the Co loading content reaches 2.4 wt%. This downturn in TONs is attributed to the formation of Co-derived clusters or particles by excessive

Co atoms (Figure S7, Supporting Information). The form of clusters and particles dramatically reduces the utilization efficiency of Co atoms in catalytic reactions.

Given that the  $\text{Co}_1\text{-G}$  nanosheets have reached a high activity, we assess another key parameter to catalytic performance—stability. To evaluate the catalytic stability of  $\text{Co}_1\text{-G}$  nanosheets, the used catalysts are collected and redispersed in a fresh reaction solution with  $[\text{Ru}(\text{bpy})_3]\text{Cl}_2$  for cycling tests. As shown in Figure 3d, the recycled catalyst retains  $\approx 88\%$  of their original activity after five runs, each of which takes 3 h. To further prove the stability of catalyst, the catalyst after the reaction is characterized by X-ray diffraction, TEM, Fourier transform-infrared (FT-IR) spectroscopy (Figure S8, Supporting Information) and XPS (Figure S9, Supporting Information), in comparison with the fresh one. The results indicate an excellent reusability and stability of the  $\text{Co}_1\text{-G}$  nanosheets. The  $\text{Co}_1\text{-G}$  nanosheets thus successfully combine the merits of high activity attained by homogeneous catalysts and facile recyclability offered by heterogeneous catalysts, which is highly promising for realizing large-scale photocatalytic  $\text{CO}_2$  reduction.

To further understand the key role of graphene in facilitating electron transfer, steady-state photoluminescence (PL) spectroscopy is employed to examine the behavior in photoexcited electron transfer from light absorber  $[\text{Ru}(\text{bpy})_3]\text{Cl}_2$  to  $\text{Co}_1\text{-G}$  nanosheets. As shown in Figure 4a, the  $[\text{Ru}(\text{bpy})_3]\text{Cl}_2$  in aqueous solution excited at 400 nm shows a strong emission peak around 610 nm. With the addition of  $\text{Co}_1\text{-G}$  nanosheets, the PL of the excited  $[\text{Ru}(\text{bpy})_3]^{2+}$  is gradually quenched. In comparison, there is almost no influence on the light absorption of  $[\text{Ru}(\text{bpy})_3]\text{Cl}_2$  by the addition of  $\text{Co}_1\text{-G}$  nanosheets (Figure S10a, Supporting Information), which further confirms that the quenching of PL intensity should be directly caused by the promoted transfer of photoexcited electrons. Furthermore, no such PL quenching can be observed when  $\text{CoCl}_2$  is added to the  $[\text{Ru}(\text{bpy})_3]\text{Cl}_2$  aqueous solution in the absence of graphene (Figure S10b, Supporting Information). This manifests the role of graphene in promoting the charge transfer and separation, which well explains why the free  $\text{Co}^{2+}$  cations ( $\text{CoCl}_2$ ) and  $\text{Co}^{2+}$  cations adsorbed to GO ( $\text{CoCl}_2 + \text{GO}$ ) can only offer low TONs for CO production (Figure 3a).

Based on the findings, we further look into the quenching mechanism. Our control experiment shows that the PL intensity of  $[\text{Ru}(\text{bpy})_3]^{2+}$  is not quenched with various amounts of sacrificial agent TEOA (Figure S10c, Supporting Information), suggesting that the excited  $[\text{Ru}(\text{bpy})_3]^{2+}$  is directly quenched by  $\text{Co}_1\text{-G}$  nanosheets in the photocatalytic system. The quenching mechanism is further elucidated through the Stern–Volmer equation<sup>[4c,17]</sup>

$$\frac{I_0}{I} = 1 + k_q \tau_0 [Q] \quad (1)$$

where  $I_0$  and  $I$  are the PL intensities without and with a quencher, respectively,  $k_q$  is the apparent rate of quenching,  $\tau_0$  is the excited-state lifetime without a quencher, and  $[Q]$  is the quencher concentration. The Stern–Volmer plots should be linear in the case of dynamic quenching, which results from the collisional encounters between luminophore and quencher. In comparison, the static quenching, along with the formation

of charge-transfer complexes between luminophore and quencher, causes an upward curvature feature in Stern–Volmer plots.<sup>[17a]</sup> In our case, the plot for the PL intensities versus the concentration of  $\text{Co}_1\text{-G}$  nanosheets (Figure 4b) turns out to be upward curvature as fitted with the Stern–Volmer equation, indicating that the PL of  $[\text{Ru}(\text{bpy})_3]\text{Cl}_2$  is static-quenched by  $\text{Co}_1\text{-G}$  nanosheets. Thus, we propose that the transfer of photoexcited electrons from  $[\text{Ru}(\text{bpy})_3]\text{Cl}_2$  to  $\text{Co}_1\text{-G}$  nanosheets takes place through an interfacial charge-transfer process;  $[\text{Ru}(\text{bpy})_3]\text{Cl}_2$  is adsorbed to the surface of  $\text{Co}_1\text{-G}$  nanosheets through  $\pi$ – $\pi$  interactions, enabling the electron transfer. The adsorption of  $[\text{Ru}(\text{bpy})_3]\text{Cl}_2$  to the graphene is proven by the XPS (Figure S9a,d, Supporting Information) and FT-IR (Figure S8b, Supporting Information) data for the  $\text{Co}_1\text{-G}$  catalyst after the photocatalytic test.

To reveal the dynamic charge behavior, we further employ time-resolved PL decay spectroscopy to characterize the systems. The emission of singlet excited  $[\text{Ru}(\text{bpy})_3]^{2+}$  in aqueous solution follows one exponential decay with a lifetime of 359.1 ns (Figure 4c), which agrees well with the literature value ( $\approx 400$  ns).<sup>[17a,18]</sup> As  $\text{Co}_1\text{-G}$  nanosheets are added to the solution, a sharp decay of the singlet excited state is observed (Figure 4d). This decay can be fitted for a double exponential decay with a short lifetime of 0.42 ns and a long lifetime of 339.5 ns. The short lifetime corresponds to the decay for the  $[\text{Ru}(\text{bpy})_3]^{2+}$  adsorbed at  $\text{Co}_1\text{-G}$  surface, while the long lifetime can be assigned to the decay for free  $[\text{Ru}(\text{bpy})_3]^{2+}$ . The sharp decrease in lifetime (0.42 ns versus 359.1 ns) again confirms that graphene can function as an excellent electron transporter in the catalytic system and consequently significantly improve the catalytic performance. As demonstrated by PL spectroscopy (Figure S11, Supporting Information), the behavior in photoexcited electron transfer from light absorber  $[\text{Ru}(\text{bpy})_3]\text{Cl}_2$  to the graphene is largely maintained by excluding the anchored Co atoms. This indicates that the coordination of single Co atoms with graphene does not obviously change its electron transfer property.

In terms of charge transfer, the band structure alignment between  $[\text{Ru}(\text{bpy})_3]\text{Cl}_2$  and  $\text{Co}_1\text{-G}$  nanosheets should be a key parameter. As indicated by UV-vis–IR diffuse reflectance spectroscopy characterization (Figure S12a, Supporting Information), the  $\text{Co}_1\text{-G}$  nanosheets do not show an absorption edge, indicating that they are a class of zero-bandgap materials—a typical feature for graphene.<sup>[19]</sup> This result indicates that the coordination of single Co atoms with graphene does not alter the band structure of graphene. The zero-bandgap feature of  $\text{Co}_1\text{-G}$  nanosheets is further evidenced by synchrotron-radiation photoemission spectroscopy (SRPES) spectroscopy. The valence-band (VB) spectrum (Figure S12b, Supporting Information) shows that the energy difference between the VB edge and the Fermi level ( $E_F$ ) is nearly zero. Meanwhile, the work function ( $\phi$ ) of  $\text{Co}_1\text{-G}$  nanosheets can be calculated to be 4.90 eV from the secondary electron cutoff ( $E_{\text{cutoff}}$ ; Figure S12c, Supporting Information) in the SRPES. In other words, the Fermi level is 4.90 eV relative to the vacuum level. Meanwhile, the highest occupied molecular orbital (HOMO) and lowest unoccupied molecular orbital (LUMO) energy levels of  $[\text{Ru}(\text{bpy})_3]\text{Cl}_2$  with respect to the vacuum level have been determined as 5.68 and 3.19 eV in previous work, respectively.<sup>[20]</sup> Given the energy level diagram

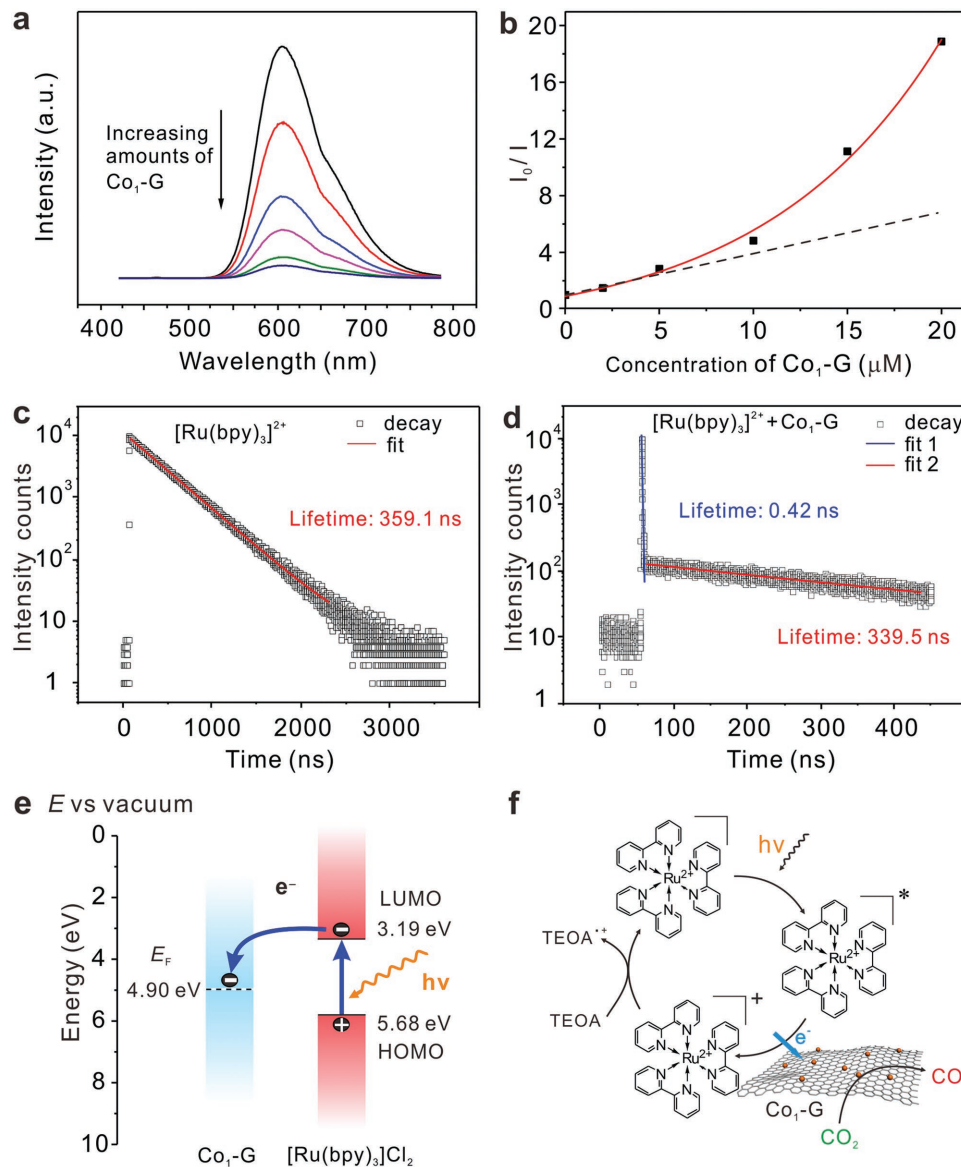


**Figure 4.** a) Steady-state PL spectra of an aqueous solution containing  $66 \times 10^{-6}$  M  $[\text{Ru}(\text{bpy})_3]\text{Cl}_2$  upon the addition of increasing amounts of  $\text{Co}_1\text{-G}$  nanosheets (0, 2, 5, 10, 15, and  $20 \times 10^{-6}$  M). The samples are excited at  $\lambda_{\text{ex}} = 400$  nm. The concentrations of  $\text{Co}_1\text{-G}$  nanosheets are given according to the contents of Co atoms. b) The plot for the PL intensities in (a) versus the concentrations of  $\text{Co}_1\text{-G}$  nanosheets, fitted with the Stern–Volmer equation. The dotted line refers to dynamic quenching. Time-resolved PL decay spectra of an aqueous solution containing  $66 \times 10^{-6}$  M  $[\text{Ru}(\text{bpy})_3]\text{Cl}_2$  c) in the absence of  $20 \times 10^{-6}$  M  $\text{Co}_1\text{-G}$  nanosheets and d) in the presence of  $20 \times 10^{-6}$  M  $\text{Co}_1\text{-G}$  nanosheets. The samples are excited by the incident light of 374 nm, while the PL decay spectra at 610 nm are monitored. e) Schematic energy-level diagram showing the electron transfer from  $[\text{Ru}(\text{bpy})_3]\text{Cl}_2$  to the  $\text{Co}_1\text{-G}$  catalyst.  $E_F$ : Fermi level; LUMO: lowest unoccupied molecular orbital; HOMO: highest occupied molecular orbital. f) Schematic process for the photocatalytic reduction of  $\text{CO}_2$  to  $\text{CO}$  using  $[\text{Ru}(\text{bpy})_3]\text{Cl}_2$  as a light absorber and  $\text{Co}_1\text{-G}$  nanosheets as a catalyst.

illustrated in Figure 4e, the Fermi level of  $\text{Co}_1\text{-G}$  nanosheets is lower than the LUMO of  $[\text{Ru}(\text{bpy})_3]\text{Cl}_2$  so that the photoexcited electrons in the LUMO of light absorber can be preferentially transferred to the Fermi level of  $\text{Co}_1\text{-G}$  nanosheets, enabling the subsequent reduction of  $\text{CO}_2$ .

As a result, the process for the photocatalytic  $\text{CO}_2$  reduction can be illustrated in Figure 4f based on our characterization results and the previous works in homogeneous systems.<sup>[4c,21]</sup> Upon photoexcitation, the light absorber  $[\text{Ru}(\text{bpy})_3]^{2+}$  is promoted to the excited state. This excited state is then directly

quenched by the catalyst of  $\text{Co}_1\text{-G}$  nanosheets to form an oxidized  $[\text{Ru}(\text{bpy})_3]^{3+}$ , during which the photoexcited electrons are transferred to the isolated catalytic Co sites where  $\text{CO}_2$  molecule is activated and reduced to  $\text{CO}$ . The oxidized light absorber is reduced back to  $[\text{Ru}(\text{bpy})_3]^{2+}$  by the sacrificial reductant TEOA to form an entire cycle. To verify the versatility of our heterogeneous single-atom Co catalyst, we have employed a robust and significantly cheaper polymeric semiconductor, graphitic carbon nitride ( $\text{g-C}_3\text{N}_4$ ), as a visible-light absorber for integration with our  $\text{Co}_1\text{-G}$  nanosheets (Figure S13,

Supporting Information). As shown in Figure S14 (Supporting Information), the  $\text{g-C}_3\text{N}_4@\text{Co}_1\text{-G}$  system can achieve effective and sustainable  $\text{CO}_2$  reduction under visible irradiation. Overall, our designed  $\text{Co}_1\text{-G}$  nanosheets play dual important roles in the photocatalytic system: (i) hosting the single-atom Co sites for catalytic  $\text{CO}_2$  reduction; and (ii) accepting electrons from the light absorber and facilitating the transfer of the received electrons to catalytic sites toward  $\text{CO}_2$  reduction.

In summary, we have developed a highly efficient photocatalytic system for  $\text{CO}_2$  reduction by bridging the heterogeneous single-atom Co catalyst with homogeneous light absorber  $[\text{Ru}(\text{bpy})_3]\text{Cl}_2$  through graphene. The developed heterogeneous single-atom catalysts well bridge the gap between heterogeneous and homogeneous photocatalysts, and thus combines their merits of high activity and robustness. As a result, the isolated Co atoms coordinated with graphene can serve as a highly active and sustainable catalyst for  $\text{CO}_2$  conversion with outstanding TON and TOF. The demonstrated roles of graphene in metal-support interactions and electron transfer highlight the importance of charge kinetics to photocatalysis, particularly when the heterogeneous and homogeneous photocatalysts are bridged. This work not only puts forward a promising strategy for developing high-performance heterogeneous photocatalysts by engineering single-atom catalytic sites, but also provides insights into charge kinetics toward efficient photocatalytic  $\text{CO}_2$  reduction.

## Experimental Section

**Synthesis of  $\text{Co}_1\text{-G}$  Nanosheets:** An aqueous suspension of graphene oxide ( $\text{GO}$ , 2 mg  $\text{mL}^{-1}$ ) was first sonicated for 3 h. Subsequently 50  $\mu\text{L}$  of aqueous  $\text{CoCl}_2\cdot 6\text{H}_2\text{O}$  solution (3 mg  $\text{mL}^{-1}$ ) was added to 2.5 mL of  $\text{GO}$  suspension, followed by sonication for 15 min and shaking for 15 min (Step 1). The precursor solution was then freeze-dried to yield a brown sample (Step 2). The obtained sample was annealed at 550 °C for 3 h under Ar protection (Step 3), which converted the  $\text{GO}$  into reduced graphene oxide (namely,  $\text{Co}_1\text{-G}$ ). After cooling to room temperature under Ar protection, the final product of black  $\text{Co}_1\text{-G}$  nanosheets was obtained. The control sample of graphene ( $\text{G}$ ) was synthesized by following the same procedure except the absence of  $\text{CoCl}_2\cdot 6\text{H}_2\text{O}$  (i.e., modified Step 1). The control sample of  $\text{CoCl}_2 + \text{GO}$  was obtained with the same procedure as  $\text{Co}_1\text{-G}$  by skipping the annealing process (i.e., skipped Step 3 for  $\text{GO}$  reduction and  $\text{Co}^{2+}$  coordination). To prepare the control sample of  $\text{CoCl}_2 + \text{G}$ , the obtained  $\text{G}$  sample was first dispersed in aqueous solution through sonication, followed by the addition of aqueous  $\text{CoCl}_2\cdot 6\text{H}_2\text{O}$  solution (the same amount) and the freeze-drying process (i.e., skipped Step 3 for  $\text{Co}^{2+}$  coordination).

**XAFS Characterization:** Co K-edge X-ray absorption fine structure measurements were performed at the beamline 14W1 in Shanghai Synchrotron Radiation Facility (SSRF), China. The X-ray was monochromatized by a double-crystal Si(111) monochromator. The storage ring of SSRF was operated at 3.5 GeV with the current of 300 mA. The acquired extended XAFS data were processed according to the standard procedures using the WinXAS3.1 program.<sup>[22]</sup> Theoretical amplitudes and phase-shift functions were calculated with the FEFF8.2 code using the crystal structural parameters of Co foil,  $\text{CoO}$ , and  $\text{Co}_2\text{C}$ .<sup>[23]</sup> Co K-edge XANES simulations based on self-consistent multiple-scattering theory were performed using the FEFF 8.2 code. For the exchange correlation part of the potential, the Hedin–Lundqvist model was employed with a 2 eV shift and additional broadening of 0.5 eV.

**PL Characterization:** Steady-state photoluminescence spectra were recorded on a JY Fluorolog-3-Tou Spectrometer and a FluoroMax-4 spectrophotometer (Horiba Scientific). Time-resolved PL decay spectra were collected by time-correlated single-photon counting (Horiba Scientific).

**SRPES Characterization:** Synchrotron-radiation photoemission spectroscopy experiments were performed at the Photoemission Endstation (BL10B) in National Synchrotron Radiation Laboratory (NSRL), China. The valence-band spectra were measured using synchrotron-radiation light as the excitation source with a photon energy of 168.5 eV and referenced to the Fermi level ( $E_F = 0$ ) determined from Au. The work function ( $\Phi$ ) was determined by the difference between the photon energy and the width of whole valence-band spectra. A sample bias of −10 V was applied for the secondary electron cutoff.

**Photocatalytic  $\text{CO}_2$  Reduction Measurement:** The photocatalytic experiments were carried out in a 300 mL Pyrex reactor equipped with a quartz lid (Perfect Light, China) under irradiation, coupled with gas chromatograph at 15 °C as controlled by cooling water (Figure S15, Supporting Information). The reaction system containing  $[\text{Ru}(\text{bpy})_3]\text{Cl}_2\cdot 6\text{H}_2\text{O}$  (15 mg, bpy = 2'2'-bipyridine),  $\text{Co}_1\text{-G}$  nanosheets (3 mg, 0.625  $\mu\text{mol}$  Co), and solvent (30 mL, acetonitrile/triethanolamine/ $\text{H}_2\text{O}$ , 3:1:1 vol.) was stirred with a magnetic stirrer and irradiated under a 300 W xenon lamp (SolarEdge700, China) with a 420 nm long-wave-pass cutoff filter (i.e.,  $\lambda > 420$  nm). The entire reaction setup was vacuum degassed, and then the high-purity  $\text{CO}_2$  gas was filled into the reaction setup to reach a pressure of 1 bar. The power density was measured to be 264.25 mW  $\text{cm}^{-2}$ . The amounts of CO and  $\text{H}_2$  evolved were determined using gas chromatograph (Techcomp GC-7900, China) equipped with a TDX-01 packed column.  $\text{H}_2$  was detected using a thermal conductivity detector. CO was converted to  $\text{CH}_4$  by a methanation reactor and then analyzed by a flame ionization detector. TON refers to the turnover number, defined as the moles of produced product per mole of catalytic sites. TOF refers to the turnover frequency, defined as the moles of produced product per mole of catalytic sites per minute. The isotope-labeled experiments were performed using  $^{13}\text{CO}_2$  instead of  $^{12}\text{CO}_2$ , and the products were analyzed using gas chromatography-mass spectrometry (7890A and 5975C, Agilent).  $^1\text{H}$ -NMR spectra were recorded on a Bruker Avance III 400 MHz NMR spectrometer.

## Supporting Information

Supporting Information is available from the Wiley Online Library or from the author.

## Acknowledgements

C.G. and S.C. contributed equally to this work. This work was financially supported in part by the National Key R&D Program of China (Grant No. 2017YFA0207301), 973 Program (Grant No. 2014CB848900), NSFC (Grant Nos. 21725102, 21471141, U1532135 and 21703220), CAS Key Research Program of Frontier Sciences (Grant No. QYZDB-SSW-SLH018), CAS Interdisciplinary Innovation Team, Innovative Program of Development Foundation of Hefei Center for Physical Science and Technology (Grant No. 2016FXCX003), Recruitment Program of Global Experts, CAS Hundred Talent Program, Anhui Provincial Natural Science Foundation (Grant No. 1708085QB26), China Postdoctoral Science Foundation (Grant No. BH2060000034), and Fundamental Research Funds for the Central Universities (Grant No. WK2060190064). XAFS measurements were performed at the beamline BL14W1 in the Shanghai Synchrotron Radiation Facility (SSRF), China. SRPES experiments were performed at the Photoemission Endstation in the National Synchrotron Radiation Laboratory (NSRL) in Hefei, China. We thank Prof. Ye Tao at the beamline 1W2B in the Beijing Synchrotron Radiation Facility (BSRF) for his help on transient XAFS characterization.

## Conflict of Interest

The authors declare no conflict of interest.

## Keywords

active sites, carbon dioxide conversion, electron transfer, photocatalysis, single-atom catalysts

Received: August 14, 2017

Revised: November 16, 2017

Published online:

- [1] a) D. Gust, T. A. Moore, *Science* **1989**, *244*, 35; b) M. S. Dresselhaus, I. L. Thomas, *Nature* **2001**, *414*, 332; c) N. S. Lewis, D. G. Nocera, *Proc. Natl. Acad. Sci. USA* **2006**, *103*, 15729; d) A. Listorti, J. Durrant, J. Barber, *Nat. Mater.* **2009**, *8*, 929; e) Y. Tachibana, L. Vayssieres, J. R. Durrant, *Nat. Photonics* **2012**, *6*, 511; f) D. Kim, K. K. Sakimoto, D. Hong, P. Yang, *Angew. Chem., Int. Ed.* **2015**, *54*, 3259.
- [2] a) W. Kim, G. Yuan, B. A. McClure, H. Frei, *J. Am. Chem. Soc.* **2014**, *136*, 11034; b) W. Tu, Y. Zhou, Z. Zou, *Adv. Mater.* **2014**, *26*, 4607; c) J. Yu, J. Low, W. Xiao, P. Zhou, M. Jaroniec, *J. Am. Chem. Soc.* **2014**, *136*, 8839; d) J. L. White, M. F. Baruch, J. E. Pander Iii, Y. Hu, I. C. Fortmeyer, J. E. Park, T. Zhang, K. Liao, J. Gu, Y. Yan, T. W. Shaw, E. Abelev, A. B. Bocarsly, *Chem. Rev.* **2015**, *115*, 12888; e) R. Kuriki, H. Matsunaga, T. Nakashima, K. Wada, A. Yamakata, O. Ishitani, K. Maeda, *J. Am. Chem. Soc.* **2016**, *138*, 5159; f) T. E. Rosser, C. D. Windle, E. Reisner, *Angew. Chem., Int. Ed.* **2016**, *55*, 7388; g) K. M. Choi, D. Kim, B. Rungtaweevoranit, C. A. Trickett, J. T. D. Barmanbek, A. S. Alshammari, P. Yang, O. M. Yaghi, *J. Am. Chem. Soc.* **2017**, *139*, 356; h) X. Qiao, Q. Li, R. N. Schauguard, B. W. Noffke, Y. Liu, D. Li, L. Liu, K. Raghavachari, L.-S. Li, *J. Am. Chem. Soc.* **2017**, *139*, 3934.
- [3] a) C. Copéret, M. Chabanas, R. Petroff Saint-Arroman, J.-M. Basset, *Angew. Chem., Int. Ed.* **2003**, *42*, 156; b) C. Copéret, A. Comas-Vives, M. P. Conley, D. P. Estes, A. Fedorov, V. Mougel, H. Nagae, F. Núñez-Zarur, P. A. Zhizhko, *Chem. Rev.* **2016**, *116*, 323; c) X. Liu, S. Inagaki, J. Gong, *Angew. Chem., Int. Ed.* **2016**, *55*, 14924; d) C. Gao, J. Wang, H. Xu, Y. Xiong, *Chem. Soc. Rev.* **2017**, *46*, 2799.
- [4] a) M. Cokoja, C. Bruckmeier, B. Rieger, W. A. Herrmann, F. E. Kühn, *Angew. Chem., Int. Ed.* **2011**, *50*, 8510; b) S. Berardi, S. Drouet, L. Francas, C. Gimbert-Surinach, M. Guttentag, C. Richmond, T. Stoll, A. Llobet, *Chem. Soc. Rev.* **2014**, *43*, 7501; c) J. Bonin, M. Robert, M. Routier, *J. Am. Chem. Soc.* **2014**, *136*, 16768; d) L. Chen, Z. Guo, X.-G. Wei, C. Gallenkamp, J. Bonin, E. Anxolabéhère-Mallart, K.-C. Lau, T.-C. Lau, M. Robert, *J. Am. Chem. Soc.* **2015**, *137*, 10918; e) Z. Guo, S. Cheng, C. Cometto, E. Anxolabéhère-Mallart, S.-M. Ng, C.-C. Ko, G. Liu, L. Chen, M. Robert, T.-C. Lau, *J. Am. Chem. Soc.* **2016**, *138*, 9413.
- [5] a) P. McMorn, G. J. Hutchings, *Chem. Soc. Rev.* **2004**, *33*, 108; b) Q. Yin, J. M. Tan, C. Besson, Y. V. Geletii, D. G. Musaev, A. E. Kuznetsov, Z. Luo, K. I. Hardcastle, C. L. Hill, *Science* **2010**, *328*, 342; c) W. Wang, S. Wang, X. Ma, J. Gong, *Chem. Soc. Rev.* **2011**, *40*, 3703.
- [6] B. Qiao, A. Wang, X. Yang, L. F. Allard, Z. Jiang, Y. Cui, J. Liu, J. Li, T. Zhang, *Nat. Chem.* **2011**, *3*, 634.
- [7] a) J. Jones, H. Xiong, A. T. DeLaRiva, E. J. Peterson, H. Pham, S. R. Challa, G. Qi, S. Oh, M. H. Wiebenga, X. I. Pereira Hernández, Y. Wang, A. K. Datye, *Science* **2016**, *353*, 150; b) P. Liu, Y. Zhao, R. Qin, S. Mo, G. Chen, L. Gu, D. M. Chevrier, P. Zhang, Q. Guo, D. Zang, B. Wu, G. Fu, N. Zheng, *Science* **2016**, *352*, 797; c) X.-F. Yang, A. Wang, B. Qiao, J. Li, J. Liu, T. Zhang, *Acc. Chem. Res.* **2013**, *46*, 1740; d) G. Gao, Y. Jiao, E. R. Waclawik, A. Du, *J. Am. Chem. Soc.* **2016**, *138*, 6292; e) R. Lang, T. Li, D. Matsumura, S. Miao, Y. Ren, Y. T. Cui, Y. Tan, B. Qiao, L. Li, A. Wang, X. Wang, T. Zhang, *Angew. Chem., Int. Ed.* **2016**, *55*, 16054; f) X. Li, W. Bi, L. Zhang, S. Tao, W. Chu, Q. Zhang, Y. Luo, C. Wu, Y. Xie, *Adv. Mater.* **2016**, *28*, 2427; g) B. Zhang, H. Asakura, J. Zhang, J. Zhang, S. De, N. Yan, *Angew. Chem., Int. Ed.* **2016**, *55*, 8319; h) H. Zhang, J. Wei, J. Dong, G. Liu, L. Shi, P. An, G. Zhao, J. Kong, X. Wang, X. Meng, J. Zhang, J. Ye, *Angew. Chem., Int. Ed.* **2016**, *55*, 14310.
- [8] S. Gao, Y. Lin, X. Jiao, Y. Sun, Q. Luo, W. Zhang, D. Li, J. Yang, Y. Xie, *Nature* **2016**, *529*, 68.
- [9] a) P. Hu, Z. Huang, Z. Amghouz, M. Makkee, F. Xu, F. Kapteijn, A. Dikhtarenko, Y. Chen, X. Gu, X. Tang, *Angew. Chem., Int. Ed.* **2014**, *53*, 3418; b) L. Wang, H. Li, W. Zhang, X. Zhao, J. Qiu, A. Li, X. Zheng, Z. Hu, R. Si, J. Zeng, *Angew. Chem., Int. Ed.* **2017**, *56*, 4712.
- [10] S. Chen, J. Zhu, X. Wu, Q. Han, X. Wang, *ACS Nano* **2010**, *4*, 2822.
- [11] a) C. Mattevi, G. Eda, S. Agnoli, S. Miller, K. A. Mkhdyan, O. Celik, D. Mastrogiovanni, G. Granozzi, E. Garfunkel, M. Chhowalla, *Adv. Funct. Mater.* **2009**, *19*, 2577; b) Z. Wei, D. Wang, D. Kim, S. Y. Kim, Y. Hu, M. K. Yakes, A. R. Laracuente, Z. Dai, S. R. Marder, C. Berger, W. P. King, W. A. de Heer, P. E. Sheehan, E. Riedo, *Science* **2010**, *328*, 1373.
- [12] Y. Chen, H. Ge, L. Wei, Z. Li, R. Yuan, P. Liu, X. Fu, *Catal. Sci. Technol.* **2013**, *3*, 1712.
- [13] a) W. Sheng, S. Kattel, S. Yao, B. Yan, Z. Liang, C. J. Hawhurst, Q. Wu, J. G. Chen, *Energy Environ. Sci.* **2017**, *10*, 1180; b) M. B. Ross, C. T. Dinh, Y. Li, D. Kim, P. De Luna, E. H. Sargent, P. Yang, *J. Am. Chem. Soc.* **2017**, *139*, 9359.
- [14] a) S. Wang, W. Yao, J. Lin, Z. Ding, X. Wang, *Angew. Chem., Int. Ed.* **2014**, *53*, 1034; b) D. J. Boston, C. Xu, D. W. Armstrong, F. M. MacDonnell, *J. Am. Chem. Soc.* **2013**, *135*, 16252.
- [15] D. Sun, Y. Gao, J. Fu, X. Zeng, Z. Chen, Z. Li, *Chem. Commun.* **2015**, *51*, 2645.
- [16] a) J. Lu, N. S. Khetrapal, J. A. Johnson, X. C. Zeng, J. Zhang, *J. Am. Chem. Soc.* **2016**, *138*, 15805; b) X. Hong, J. Kim, S.-F. Shi, Y. Zhang, C. Jin, Y. Sun, S. Tongay, J. Wu, Y. Zhang, F. Wang, *Nat. Nanotechnol.* **2014**, *9*, 682.
- [17] a) J. R. Lakowicz, *J. Biomed. Opt.* **2008**, *13*, 029901; b) V. S. Thoi, N. Kornienko, C. G. Margarit, P. Yang, C. J. Chang, *J. Am. Chem. Soc.* **2013**, *135*, 14413.
- [18] J. H. Kim, M. Lee, C. B. Park, *Angew. Chem., Int. Ed.* **2014**, *53*, 6364.
- [19] a) A. Iwase, Y. H. Ng, Y. Ishiguro, A. Kudo, R. Amal, *J. Am. Chem. Soc.* **2011**, *133*, 11054; b) H. Chang, Z. Sun, Q. Yuan, F. Ding, X. Tao, F. Yan, Z. Zheng, *Adv. Mater.* **2010**, *22*, 4872.
- [20] a) C. Gao, Q. Meng, K. Zhao, H. Yin, D. Wang, J. Guo, S. Zhao, L. Chang, M. He, Q. Li, H. Zhao, X. Huang, Y. Gao, Z. Tang, *Adv. Mater.* **2016**, *28*, 6485; b) D. A. Bernards, S. Flores-Torres, H. D. Abruña, G. G. Malliaras, *Science* **2006**, *313*, 1416.
- [21] a) A. J. Morris, G. J. Meyer, E. Fwujita, *Acc. Chem. Res.* **2009**, *42*, 1983; b) J. Schneider, H. Jia, J. T. Muckerman, E. Fujita, *Chem. Soc. Rev.* **2012**, *41*, 2036; c) Y. Kou, Y. Nabetani, D. Masui, T. Shimada, S. Takagi, H. Tachibana, H. Inoue, *J. Am. Chem. Soc.* **2014**, *136*, 6021.
- [22] T. Ressler, *J. Synchrotron Radiat.* **1998**, *5*, 118.
- [23] A. L. Ankudinov, B. Ravel, J. J. Rehr, S. D. Conradson, *Phys. Rev. B* **1998**, *58*, 7565.